CDF Note 247
August 31, 1984

Study of Electromagnetic Showers in the CDF Central Electromagnetic Calorimeter Strip Chamber

Nickolas Solomey
and
A. Barry Wicklund
Argonne National Laboratory

1. Introduction

The CDF central electromagnetic calorimeter is a lead-scintillator sandwich instrumented with a wire proportional chamber, commonly known as the strip chamber, located near shower maximum. The main purpose of this chamber is to provide good position resolution on electron and photon showers and to allow separation of multiple showers in a single tower. The chamber provides pulse height readout in two orthogonal directions; the anode wire channels give the shower pulse height distribution as a function of the production azimuth, ϕ, and the cathode strips give the shower profile along the rapidity axis (i.e. the polar angle, θ.) The close pulse height correlation between the anode and cathode wires resolves the ambiguity in θ-ϕ matching when multiple showers are present. Our analysis, based on test beam data on five wedge modules covering a full range of angles and energies from 10 to 100 GeV, indicates that position resolutions of 1 to 3 mm can be achieved, depending on energy, with a single algorithm that is independent of energy and position, and that applies equally to cathode and anode views. The overall energy resolution of the chamber is poor in comparison with the scintillator resolution, since it represents a single shower sample; it is important for energy measurement when multiple showers occur in a single tower, and also for

electron/hadron separation. We find that the resolution and response are fairly uniform in angle, but that the response is nonlinear with energy. The energy resolution is 20 to 30%, depending on energy.

The construction details of the strip chamber are summarized in Table I-1. Briefly, the chamber covers all ten towers in a single calorimeter wedge, that is, $\pm 7.5^{o}$ in ϕ and $40\text{-}90^{o}$ in θ. The anode wire cells are separated by aluminum extrusions and are ganged together pairwise to form 64 logical cells, each 14.53 mm in width; the anode wires are split in length so as to give 32 readout channels each on the "45°" and "90°" halves of the wedge (38° - 53° and 53° - 90° mrad, respectively). There are a total of 128 cathode strip channels, 59 on the "45°" half, and 69 on the "90°" half, with strip widths 20.07 mm and 16.67 mm, respectively. In both views, an electromagnetic shower is typically confined within five cells.

We describe the results of our analysis in Sections II and III below and summarize our findings in Section IV. Section II describes the overall energy response and resolution, and Section III examines the more complicated problem of shower localization, based on analysis of shower shapes and fluctuations. Section III also takes up the measurement of the incident electron position with the test beam, and the coordinate transformations that are needed to compare strip and wire views.

II. Energy Reponse

The normalized strip chamber pulse height, defined as

$$(P/E)/(P_{50}/50) \quad ,$$

is plotted against electron energy in Fig. 1 (here P is the pulse height, E the electron energy). The data in Fig. 1 are for tower 1, but the same energy dependence is seen in the other towers. The normalized pulse height falls more rapidly with energy than was observed in the CDF prototype (L. Nodulman

et al., Nucl. Instr. and Meth. 204, 351 (1983)). The two curves in Fig. 1 show the expected energy dependence for the number of shower electrons at shower depths of 5 and 6 r.l., respectively, based on the parameterization of Müller (D. Müller, Phys. Rev. 5, 2677 (1972)). Müller's fits to the longitudinal shower development are shown in Fig. 2. The strip chamber is nominally located at a depth of 5.9 r.l. in Tower 1, including the solenoidal coil; the depth is the same in Towers 0-8 within ±0.2 r.l. The relation between the data and the curves of Fig. 2 suggests that the strip chamber may be closer to ~ 5.5 r.l., rather than 5.9 r.l. in the test beam setup. Note that the depth for shower maximum for electrons is given by Müller as

$$t_{max} = 6.2 + \ell n(E/10) \text{ r.l.} \qquad \text{II-1}$$

The rms widths of the electron energy distributions are shown in Fig. 3. They vary from ~ 30% at 10 GeV to ~ 20% at 100 GeV. We might expect the sampling fluctuations to vary as

$$\frac{\sigma(P)}{P} \propto F(t/t_{max}) \times \frac{1}{\sqrt{P}} \quad , \qquad \text{II-2}$$

where F is minimal at $t = t_{max}$, and increases for $t_{max} > t$ due to fluctuations in shower origin. It is obvious that the resolution falls much more gradually with energy than simply $P^{-1/2}$; for example, extrapolating from 10 GeV, $P^{-1/2}$ behavior would yield 10% resolution at 100 GeV, to be compared with 22% observed. If the discrepancy is attributed $F(t/t_{max})$ in Eq. II-2, we would require a strong variation in F: e.g. $F(0.65)/F(0.89) \sim 1.7$. If t/t_{max} were in fact close to unity (at all energies), such a variation would seem unreasonable.

The dependence of the average pulse height on angle, for fixed electron energy (50 GeV), is shown in Fig. 4. Since the radiation depth is designed to be independent of θ (within ±0.2 r.l.), the main source of variation in P/E with θ should be the $1/\sin\theta$ dependence of the strip-chamber gas thickness seen by the shower secondaries. Indeed, this seems to be consistent with the data of Fig. 4.

Table I-1 Strip Chamber Geometry

Perpendicular distance to beamline 185 cm
Wire channels (64)
There are 62 cells in the extrusion. They are ganged in pairs except at edges:

0112233 . . . 001 (add 32 other side)

The wires are split at the tower 4-5 boundary which is also the strip width change
The logical wire boundary separation is 1.453 cm
The total width is 45 cm, 15 degrees implies 48.7 cm
The wire 15-16 (47-48) boundary is centered
Readout is through 200 pF

Strip channels (128)
Corresponding to wires 0-31 towers 0-4
69 strips of width 1.667 cm (0-68)
Begins 6.16 cm, ends 121.16 cm
(from 90 degree outside steel face)
Corresponding to wires 32-63 towers 5-9
59 strips of width 2.007 cm (69-127)
Begins 121.16 cm, ends 239.56 cm

Overall placement error +/- 1.0 mm both dimensions

Physical characteristics
Cell 0.250 in. deep by 0.239 in. wide
Walls 0.047 in. thick (16.4%)
Wire 0.002 in. gold plated tungsten
Total thickness 0.75 in.
0.069 radiation lengths
0.022 absorption lengths

High voltage
Separate feedin for each logical wire channel from 4 external boxes (at each corner)
One box has an input filter and test point for putting pulses on the wires
1 M ohm feedin on chamber and 100 k ohm in box for debug

Gas
Parallel flow internally manifolded
Two input and two output 1/4 in. black polyflo
(no preferred end)

Finally, the rms width of the electron energy distributions, at 50 GeV fixed energy, is shown as a function of angle in Fig. 5. There appears to be a systematic decrease in $\sigma(P)/P$ with decreasing θ; $\sigma(P)/P \simeq 26\%$ at 90°, and $\sim 22\%$ at 40°. Note that the dependence of $F(t/t_{max})$ deduced above is such that an increase of .05 in t/t_{max} over the θ range (i.e. 0.4 r.l.), would result in an $\sim$ 15% improvement in resolution, close to what is observed. Alternatively, the θ dependence of the resolution might be due to the $1/\sin\theta$ increase in track length (i.e. statistics on primary ionization electrons) rather than shower fluctuations.

III. Position Determination

Coordinate Systems

Figure 6 illustrates the coordinate system plan view. The strip chamber is located in the x-y plane at a fixed distance, z = 1.812 m, along the z-axis from the final beam proportional chamber. The beam PWC's 1, 2, and 3 are positioned along the z' axis at z' = -48.92m, -26.67m, and 0m, respectively. For $\theta = 90^o$, z and z' axes are the same. The strip chamber wire channels are defined by extrusion boundaries at $y = y_i$, $y_i + \Delta$, $y_i + 2\Delta$ ... (Δ = 14.53 mm). The cathode strip boundaries are fixed at $x = x_i$, $x_i + \Delta'$, $x_i + 2\Delta'$ ... (Δ' = 16.67 mm for i = 1 -- 69, and 20.07 mm for i = 70 -- 128). For our purposes, the electron trajectory is characterized by

$$dx/dz \simeq 1/\cot\theta$$
$$dy/dz \simeq 0 \quad . \qquad \text{III-1}$$

It is important to note that the electron shower is presumably symmetric about the beam axis, z', and therefore has a characteristic oblate shape projected onto the strip chamber plane. That is, if the shower size is given by σ tranverse to z', then the size in the strip chamber will be

$$\sigma_y = \sigma \text{ (wire channel view)}$$

$$\sigma_x = \sigma/\sin\theta \text{ (strip channel view)} \quad . \qquad \text{III-2}$$

Note that the shower profile could, in principle, vary with θ, because the effective density of the radiator stack decreases as $\sin\theta$ (the number of radiation lengths is fixed but the stack dimension increases as $1/\sin\theta$); thus we might expect slightly fatter showers at 45° than at 90°. The relation between strip and wires views should be given in Eq. III-2 in any case.

A further potential complication should be noted (it turns out to be negligible in practice). In the anode wire view, the wire pulse height should reflect simply the number of shower secondaries contained within the channel extrusion boundaries. However, in the cathode strip view, the pulse height is not given simply by the number of secondaries within the strip boundaries. Rather, the strip pulse height is induced by the charge distribution along the wire, and the charge induced as a function of x is given by

$$P_s(x) = \int_{-\infty}^{\infty} dx' \; \rho_s(x-x') \; P(x') \quad . \qquad \text{III-3}$$

Here P_s is the shower profile observed in the strip view, $P(x)$ is the actual shower distribution, and $\rho_s(x)$ can be deduced from the chamber geometry, and has been measured with the chamber test stand. Thus, interpretation of the strip data is complicated both by the projective geometry and by the sharing function, $\rho_s(x)$. The wire channels provide a more direct view of shower characteristics.

Beam PWC Contribution to Position Resolution

The vertical coordinate of the beam at the strip chamber plane is given by

$$y = y_3 + \left(\frac{y_3 - y_2}{z_3' - z_2'}\right) \times \frac{1.812}{\sin\theta} \quad , \qquad \text{III-4}$$

where $y_{1,2,3}$ are the PWC coordinates, and $z'_{1,2,3}$ are as given above. With 1 mm wire spacing, we would expect ±0.3 mm digitization accuracy. To estimate multiple scattering contributions, we measured the rms deviation of [y_1, y_2, y_3] from a straight line, as a function of energy. The resolution on Δy_2, defined as

$$\Delta y_2 = y_2 - \left[y_1 + \left(\frac{y_3 - y_1}{z'_3 - z'_1}\right) \cdot (z'_2 - z'_1)\right] \quad , \qquad \text{III-5}$$

is listed in Table III-1, together with the observed rms beam divergences.

Table III-1

E	Δy_2 (rms)	$\frac{y_3 - y_2}{z'_3 - z'_2}$ (rms)
10 GeV	2.3 mm	0.4 mrad
25 GeV	1.2 mm	0.2 mrad
100 GeV	0.8 mm	0.24 mrad

A rough interpolation of the y_2 resolution is given by

$$(\Delta y_2 \text{ - rms})^2 \simeq (0.7 \text{ mm})^2 + \left(\frac{20 \text{ mm}}{p(\text{GeV})}\right)^2 \quad . \qquad \text{III-6}$$

The constant term, σ = 0.7 mm, corresponds to a single chamber resolution of ±.57 mm, somewhat worse than the 0.3 mm expected. The 20 mm/p contribution, regarded as the effect of a lumped multiple scatter at PWC-2, corresponds to a total multiple scatter rms at PWC-2 of

$$\theta^2\text{-rms} \sim (5.8 \text{ mrad}/p(\text{GeV}))^2 \qquad \text{III-7}$$

or about 15% of a radiation length. Assuming an error of half this angle in extrapolating from PWC-3 to the strip chamber, we get

$$\sigma^2(\text{y-strip}) \sim (0.6\ \text{mm})^2 + \left(\frac{5\ \text{mm}}{P \cdot \sin\theta}\right)^2 \quad . \qquad \text{III-8}$$

In quadrature, this contribution is typically only 25% of the observed resolution in the strip chamber, and so we conclude that the beam PWC resolution is ignorable in our subsequent analysis.

Shower Properties

We can characterize the shower profile, projected on the y axis, by an average shape, P(y), and fluctuations. The wire channel pulse heights are given, on average, by

$$Q_i = q \int_{y_i}^{y_i+\Delta} P(y-y_e)dy \quad , \qquad \text{III-9}$$

where q is the total charge, y_e is the electron coordinate (measured with the beam PWC's) and $[y_i, y_i + \Delta]$ define the wire channel boundaries. The normalized wire channel charges are defined by

$$\tilde{Q}_i = Q_i / \Sigma\ Q_i \quad , \qquad \text{III-10}$$

(P(y) has unit integral). A typical event $\tilde{Q}_i$ distribution is shown in Fig. 7. About ~ 70% of the charge is contained in the central wire, and five channels are sufficient to contain ~ 95% of the total charge.

We can determine P(y) indirectly from the integral function

$$I(y) = \int_{-\infty}^{y} P(y')dy' \quad , \qquad \text{III-11}$$

and

$$P(y) = \frac{d}{dy} I(y) \quad . \qquad \text{III-12}$$

For a given event, I(y) can be determined for each of the five wire channels,

$$I(y_N - y_e) = \left(\sum_{i=1}^{N-1} Q_i\right) / \left(\sum_{i=1}^{\infty} Q_i\right) \quad . \qquad \text{III-13}$$

Figure 8 shows a scatter plot of $I(y_N - y_e)$ with N = 1 -- 5 entries for each event. We fit I(y) to an analytic function and thereby determine P(y) by taking the derivative. In the cathode strip view, we have noted that, for a given shower shape, the projected shower distribution is stretched out by $1/\sin\theta$ along the x-axis (cf. Eq. III-2); in addition, the observed charge distribution is smeared out by the function $\rho_s(x-x')$ introduced above (Eq. III-3). Thus, it can be shown that the observed charge distribution in the strip view, given a canonical shower profile P(y), is given by

$$I_s(x-x_e) = \int_{-\infty}^{\infty} dx'\ I\left[(x'-x_e)\cdot\sin\theta\right]\cdot\rho_s(x-x') \quad . \qquad \text{III-14}$$

Figure 9(a) shows P(y) deduced from a typical fit to the anode wire data, and Fig. 9(b) shows the strip smearing function $\rho_s(x)$. Figure 9(c) shows $I(y-y_e)$ for the wire view; also shown is the difference $I_s(x-x_e) - I(x-x_e)$ for $\theta = 90^o$ caused by the smearing function. This difference is small, and for simplicity we have done the strip view analysis using

$$I_s(x-x_e) \simeq I\left[(x-x_e)\cdot\sin\theta\right] \quad . \qquad \text{III-15}$$

As for the analytic functions used to fit I(y) and P(y), we have tried two reasonable forms

$$P(y-y_e) = \frac{1}{\sigma}\, e^{-(y-y_e)/\sigma}\ ,\ \sigma \simeq 7\ \text{mm} \quad , \qquad \text{III-16}$$

and

$$y-y_e = Y[I] = K\left[a_1 \tan\left[\pi\ (I-\tfrac{1}{2}) + a_2[I-\tfrac{1}{2}] + a_3[I-\tfrac{1}{2}]^3\right]\right] . \qquad \text{III-17}$$

We will refer to III-16, III-17 as parameterizations 1 and 2. Parameterization 1 was suggested by Jensen and Yasuoka. Parameterization 2, which we have used for most subsequent analysis, has the advantage that it inverts the relation between $y-y_e$ and $I(y-y_e)$ and thus allows speedy estimation of y_e, given the normalized charges for a given event. Parameterization 2 can be inverted to yield $I(y-y_e)$ and $P(y-y_e)$ as shown in Fig. 9.

Pulse Height Weighted Position Determinations

The usual algorithm for obtaining the electron coordinate, y_e, would be by pulse height weighting, e.g.

$$\tilde{y}_e^n = \sum_{i=1}^{N} \frac{\bar{y}_i \, Q_i^n}{\sum_{i=1}^{N} Q_i^n} \quad , \qquad \text{III-18}$$

where $\bar{y}_i$ is the central coordinate for channel i in an event, and n = 1,2,... . Since we have an analytic expression for P(y) and Q_i (Eq. III-9), we can evaluate the difference between the estimated $\tilde{y}_e^n$ and true electron coordinate y_e, as a function of y_e. This is shown in Fig. 10 for parameterizations 1 and 2 and for n = 1,2. When y_e falls on a channel center or channel edge, the error is zero (this is clear from symmetry), but otherwise the pulse height weighting moves $\tilde{y}_e^n$ systematically closer to the channel center. This is also seen in the data. Figure 11(a) shows $\tilde{y}_e^{n=2}$ plotted against y_e (the spread is, of course, caused by shower fluctuations from the average shape). A distinct "stair step" is observed, corresponding to the systematic deviations of Fig. 10, and the rms resolution on $\tilde{y}_e^n - y_e$ suffers accordingly (Fig. 11(b)). Figure 12(a) shows the same plot using an unbiased fit of the pulse height Q_i to the canonical shower shape. The linearity between this estimate and measured y_e is restored, and the resolution is improved accordingly (Fig. 12(b)).

Least Squares Position Determination

It is obvious that the best determination of the electron coordinate can be achieved with a least squares fit, using $P(y-y_e)$ to fix the shower shape, and using an error matrix that reflects the shower fluctuations and channel-to-channel correlations. The starting point for the fit is given by

$$\chi^2 = \sum_{i=1}^{N} \sum_{j=1}^{N} \left[Q_i - Q[y_i, y_e, q]\right] \left[Q_j - Q[y_j, y_e, q]\right] \cdot G_{ij}^{-1} \quad , \qquad \text{III-19}$$

where the error matrix,

$$G_{ij} = < \delta Q_i \ \delta Q_j > \qquad \text{III-20}$$

is itself, a priori, a function of y_e (more precisely, of the location of y_e with respect to the channel edges, y_i). The fit minimizes χ^2 with respect to y_e, the desired coordinate, and q, the total charge, using N ≃ 5 wire channels, or any subset of these channels.

It is clear that the error matrix can be factored into two contributions. First, there can be an overall charge fluctuation which preserves the shower shape. This amounts to a scale error on the Q_i and governs the resolution on q (~ ±25%); this overall scale fluctuation cannot affect y_e in the fit. Second, there can be shape fluctuations, which are responsible for the resolution on y_e. Thus G_{ij} can be replaced by

$$G_{ij} \rightarrow < \delta\tilde{Q}_i \ \delta\tilde{Q}_i > \quad , \qquad \text{III-21}$$

where $\tilde{Q}_i$ are the normalized channel charges. It is clear that the normalization condition requires strong, generally negative correlations between, e.g., $\tilde{Q}_j$ and $\tilde{Q}_{j\pm1}$. These can be measured as discussed below. We remark that the unnormalized correlations of Eq. III-20 can also be directly measured. It turns out that there are large, generally positive correlations between the fluctuations in Q_j and $Q_{j\pm1}$, due to the large overall fluctuations in the shower charge. We know of no choice of variables that would result in a truely diagonal error matrix. We discuss the determination of the error matrix in more detail below.

In the simple case that we have N = 5 channels, and we arbitrarily choose a constant, diagonal error matrix, the χ^2 of Eq. III-19 is equivalent to

$$\chi^2 = \sum_{i=1}^{N} \frac{[y_i - y_e - y\ (I_i)]^2}{\sigma_i^2} \quad , \qquad \text{III-22a}$$

where

$$\sigma_i = dy/dI \ (y = y_i) \quad . \qquad \text{III-22b}$$

Here y_i are the channel boundaries, I_i is the normalized integral charge for y < y_i (Eq. III-13), and y(I) is given by parameterization 2, Eq. III-17. This ansatz is equivalent to

$$\bar{y}_e = \frac{\sum_{i=1}^{N} \left(y_i - Y(I_i)\right) \cdot 1/\sigma_i^2}{\sum_{i=1}^{N} \frac{1}{\sigma_i^2}} \quad . \qquad \text{III-23}$$

This algorithm was used for Fig. 11.

In principle, with a more accurate ansatz for the error matrix, one can improve the fit using the full χ^2 minimization. Also, if a channel happens to be unusable because of electronics problems, it may be desirable to do a χ^2 fit using a subset of the channels near the shower. We show below that such a procedure works surprisingly well. The ansatz of Eq. III-23 is not directly applicable to this problem, because it requires knowledge of all five normalized charges; one would have to iterate the procedure to take account of the missing charge, as is automatically done in the χ^2 minimization.

Results on Position Resolution

We have investigated the energy and angle dependence of the shower shape function, P(y), and have found that P(y) is independent of electron energy, total shower pulse height (q), and angle θ. As noted above, the difference between strip and wire views due to $\rho_s(x)$ is ignorable, and only the $1/\sin\theta$ spreading in the strip view needs to be taken into account. The same function appears to work well for all wedges tested so far, and is independent of elevation (ϕ) as well as θ.

We find that the position resolution is a function of the total charge, q, but is otherwise independent of primary electron energy. The position

resolution is shown as a function of pulse height in Fig. 13(a). A measure of the shower shape fluctuations is shown in Fig. 13(b), together with a $1/\sqrt{P.H.}$ interpolation. The shape fluctuation is defined as the rms spread on the normalized pulse height,

$$< \delta\tilde{Q}_i \ \delta\tilde{Q}_i >^{1/2} \quad ,$$

for the central wire channel, for events with the electron coordinate aligned with the channel center. In the Monte Carlo we can arbitrarily vary the shower fluctuation, and compare the observed central bin fluctuation with the position resolution. The two are related by a fixed ratio, and the curve in Fig. 13(a) is the Monte Carlo prediction, given the shape fluctuation in Fig. 13(b). We conclude that the position resolution which we observe is caused by the shape fluctuations, as predicted by Monte Carlo, and that these fluctuations are a function only of the shower pulse height.

Figure 14 shows the cathode and anode position resolutions versus electron energy, using the ansatz of Eq. III-23 (we have averaged over the shower pulse height). The strip view resolution is somewhat worse than the wire view, partly due to the coarser strip segmentation; we have not done Monte Carlo studies to understand this difference.

Figure 15 shows the average resolution versus angle, for fixed electron energy. The wire view resolution is flat in θ, and the strip resolution is consistent with a $1/\sin\theta$ variation. Note that the strip resolution is quoted with respect to the physical x axis (in the chamber plane). If we project back to the plane perpendicular to the electron direction, as in Fig. 6, the projected x' resolution, like the y resolution, would then be independent of θ. This is consistent with the hypothesis that the resolution is governed by shower shape fluctuations; these shape fluctuations must have a fixed size in the x'-y plane, and hence the resolution must be fixed in the x' and y directions independent of θ.

As noted above, we also tried killing selected channels and repeating the χ^2 fits. Table III-2 lists the position resolutions at 50 GeV for each channel missing (1) for the χ^2 fit, and (2) from linear pulse height averaging. The averaging process simply ignores the missing channel, and so is systematically biased as well as having poorer resolution. The χ^2 fit gives surprisingly good resolutions, and gives unbiased position (within 0.2 mm) and charge estimates.

Table III-2

Missing Channel	$\sigma(\chi^2$ fit)	σ(average)
1	1.5 mm	1.9 mm
2	2.6 mm	2.7 mm
3	2.5 mm	5.5 mm
4	2.6 mm	2.8 mm
5	1.5 mm	1.8 mm

Shower Fluctuations

We can quantify the shower shape fluctuations by using real and Monte-Carlo "data" to measure the error matrix for the χ^2 fit, namely,

$$G_{ij} = \langle (\tilde{Q}_i - \tilde{Q}\,(\bar{y}_i - y_e))\,((\tilde{Q}_j - \tilde{Q}\,(\bar{y}_j - y_e)) \rangle \quad , \qquad \text{III-24}$$

where $\tilde{Q}_i$ is the observed normalized charge in channel i, and $\tilde{Q}(\bar{y}_i - y_e)$ is the expected normalized charge, given the PWC measurement of y_e and the coordinate of the channel center, $\bar{y}_i$. Specifically, we have

$$\tilde{Q}(\bar{y}_i - y_e) = I(\bar{y}_i + \tfrac{\Delta}{2} - y_e) - I(\bar{y}_i - \tfrac{\Delta}{2} - y_e) \quad . \qquad \text{III-25}$$

We repeat our earlier observation, that G_{ij} could be defined and measured using the unnormalized charges, Q_i, in Eq. III-24. Either choice should give the same shower position for the χ^2 fit of Eq. III-19, and neither choice has

any particular advantage in eliminating correlations between neighboring channels. Rather than observe the correlations that include the overall shower charge fluctuations, we wish to focus on shape fluctuations and hence on $\tilde{Q}_i$. We remark also that we would observe larger correlations if we simply measured the averages

$$< \tilde{Q}_i \tilde{Q}_j > - <\tilde{Q}_i> <\tilde{Q}_j> \quad .$$

When we bin the data in $\bar{y}_i - y_e$, the functional dependence of $\tilde{Q}_i$ on $\bar{y}_i - y_e$ gives intrinsic correlations with this definition. Eq. III-24 allows us to observe true fluctuations about the expected function $\tilde{Q}(\bar{y}_i - y_e)$, with finite bins in $\bar{y}_i - y_e$.

Figure 16 shows two examples of such correlations as a function of $\bar{y}_i - y_e$. For ease of display, we have defined these as

$$\text{"}< \tilde{Q}_n \tilde{Q}_n >^{1/2}\text{"} = \sqrt{G_{nn}}$$

$$\text{"}< \tilde{Q}_n \tilde{Q}_{n-1} >^{1/2}\text{"} = \frac{G_{nn-1}}{\sqrt{|G_{nn-1}|}} = <\tilde{Q}_{n-1} \tilde{Q}_n>^{1/2} \quad . \qquad \text{III-26}$$

$G_{nn} G_{n-1} G_{n-1}$

The (n n-1) correlations are negative because of the normalization condition on the $\tilde{Q}_n$. Note that the correlations have the same overall dependence on $\bar{y}_i - y_e$ from 10 to 100 GeV. We show the Monte Carlo prediction for the shape of these correlation functions together with the 100 GeV data (Figs. 16(e) and (j)). By increasing the scale of the fluctuations as $1/\sqrt{P.H.}$ we can trivially obtain the lower energy behavior. What is important is that, given Monte Carlo fluctuations that match the measured G_{nm}, we can predict the position resolution, and we find that the predicted position resolution scales with G_{nm} just as in the observed data, as noted in Fig. 13.

The Monte Carlo fluctuations are generated by choosing

$$Q_n = Q_o \cdot \left[\tilde{Q}(\bar{y}_n - y_e) + \delta_1^n + \delta_2^n \sqrt{\tilde{Q}(\bar{y}_n - y_e)}\right] \quad , \qquad \text{III-27}$$

where δ_1^n = Ranf $(-\delta_1, \delta_1)$ and
δ_2^n = Ranf $(-\delta_2, \delta_2)$,
Q_o is the (Gaussian distributed) overall shower charge.

For the 100 GeV Monte Carlo, we chose $\delta_1 = .028\sqrt{3}$, $\delta_2 = .08\sqrt{3}$. The $\tilde{Q}_n$ are then obtained by normalizing the Q_n of Eq. III-27; thus, for $\delta_1^n = \delta_2^n = 0$, we would get $\tilde{Q}_n = \tilde{Q}(y_n - y_e)$. By assumption the δ_1^n, δ_2^n fluctuations are independent for each channel, and the channel correlations on $\tilde{Q}_n$ arise from the normalization condition. After some algebra, we can show, to order $(\delta^n)^2$

$$\langle \tilde{Q}_n \rangle = \tilde{Q}(y_n - y_e) - \left[\delta_1^2 + \tilde{Q}(y_n - y_e)\delta_2^2\right] \quad , \qquad \text{III-28}$$

WRONG

and

$$\langle G_{nm} \rangle = \delta_{nm}\left[\delta_1^2 + \delta_2^2 \tilde{Q}_n\right] + \tilde{Q}_n \tilde{Q}_m \left[5\delta_1^2 - \delta_2^2\right] - (\tilde{Q}_n + \tilde{Q}_m)\delta_1^2 \quad , \qquad \text{III-29}$$

where δ_{nm} is the Kronecker delta function, not to be confused with δ_1, δ_2. Actually, Eq. III-29 is an approximation because we truncate the fluctuations so that the pulse heights are non-negative, and also the beam digitization of 1 mm is included in the the Monte Carlo. However, Eq. III-29 shows the general dependence on δ_1, δ_2. The fluctuation in G_{nn} at the peak height ($\bar{y}_n \sim y_e$) is dominated by the $\delta_2^2 \tilde{Q}_n$ contribution, while the correlations for $n \neq m$ are necessarily negative unless $5\delta_1^2 > \delta_2^2$.

Figure 16-k shows the expected pulse height distribution for $\tilde{Q}(y_n - y_e)$ as a function of $y_n - y_e$. This is not identical to the shower profile $P(y-y_e)$, in that $\tilde{Q}$ integrates over a wire channel. Nevertheless, the distribution is much narrower than the correlation distributions; that reflects the $\sqrt{Q}$ dependence

of the δ_2 fluctuation. Figures 16-1 through 16-p show the average deviations of the observed $\tilde{Q}$ from the predicted values. Note that the deviation is expected to be negative, from Eq. III-28, by .01 to .05 depending on pulse height. There is no strong energy dependence in this difference, however, and we conclude that the shower shape is independent of energy within a few percent (also, the constants we have used could be tuned up to account for these differences).

Summary

We have investigated the pulse height response and shower position determination in the CDF strip chamber. The pulse height response is consistent with expected electron shower profiles. The angular dependence of the pulse height response is consistent with $1/\sin\theta$ expected from geometry.

The shower profile seems to be consistent with a universal shape which is independent of energy and angle, viewed in the plane perpendicular to the electron direction. The position resolution achieved so far behaves as (Pulse Height)$^{-1/2}$, and is around 1.1 mm at 100 GeV in the wire view, the strip resolution being slightly worse. Viewed in the plane perpendicular to the electron direction, the resolution is independent of θ. Monte Carlo simulations predict a fixed ratio between the observed shower fluctuations and the position resolution, and the Monte Carlo predictions for this ratio are consistent with observation. The shower fluctuations can be characterized by random, independent fluctuations in each of the channels, of the form $\delta_1 + \delta_2 \sqrt{\text{Pulse Ht.}}$; the magnitude of this fluctuation is around ±12% at 100 GeV at the peak center. A fast position finding algorithm has been tested. Conceivably the resolution could be further improved by introducing the true error correlation matrix in the position fit. We have noted that even in the worst case, with a dead channel, we can achieve ±2.7 mm resolution (at 50 GeV) with our present χ^2 fit.

Figure Captions

Fig. 1 Normalized strip chamber pulse height $(P/E)/(P_{50}/50)$. The curves give the expected response for electron showers with the strip chamber at 5 and 6 r.l., respectively. The chamber is nominally at 5.9 r.l.

Fig. 2 Shower profiles in the energy region 2 to 1024 GeV from D. Müller, Phys. Rev. 5, 2677 (1972); see CDF Note-27.

Fig. 3 RMS half-width of the electron energy distribution as a function of initial electron energy.

Fig. 4 Dependence of the average pulse height on angle, for fixed electron energy (50 GeV).

Fig. 5 RMS half-width of the electron energy distribution at 50 GeV fixed energy as a function of angle.

Fig. 6 Coordinate beam line system for wedge.

Fig. 7 $\tilde{Q}_i$ distribution for a typical event.

Fig. 8 Scatter plot of $I(Y_n - Y_e)$ with 5 entries for each event.

Fig. 9 (a) P(y) deduced from a typical fit to the anode wire data, (b) strip smearing function, (c) $I(y-y_e)$ for the wire view, and difference $I_s(x - x_e) - I(x - x_e)$ for $\theta = 90^o$ caused by smearing function.

Fig. 10 Evaluation of difference between the estimated $\tilde{Y}_e^n$ and true electron coordinate y_e, as a function of y_e, for position determination by P.H. squared weighting and P.H. weighting. The solid (dashed) curves are based on parameterizations (1,2) described in the text.

Fig. 11 (a) Shower position using P.H. squared weighting $\bar{y}^{n=2}$ plotted against true electron position y_e, (b) position resolution, $\bar{y}^{n=2} - y_e$, in strip chamber with pulse height squared weighting.

Fig. 12 (a) Shower position using χ^2 fit, $\bar{y}$ plotted against true electron position y_e, (b) shower position resolution, $\bar{y} - y_e$, in strip chamber using χ^2 fit.

Fig. 13 (a) The position resolution as a function of pulse height; the curve shows Monte Carlo prediction, (b) shower shape fluctuations together with $1/\sqrt{\text{P.H.}}$ interpolation.

Fig. 14 The cathode and anode position resolution versus initial electron energy.

Fig. 15 Average position resolution versus angle, for a fixed electron energy of 50 GeV.

Fig. 16 (a-j) Shower shape fluctations at 10, 25, 37.5, 50 and 100 GeV (see text for definition); (r) expected $\tilde{Q}$ versus positron; (l-p) systematic differences between observed and expected $\tilde{Q}$ for the five energies.

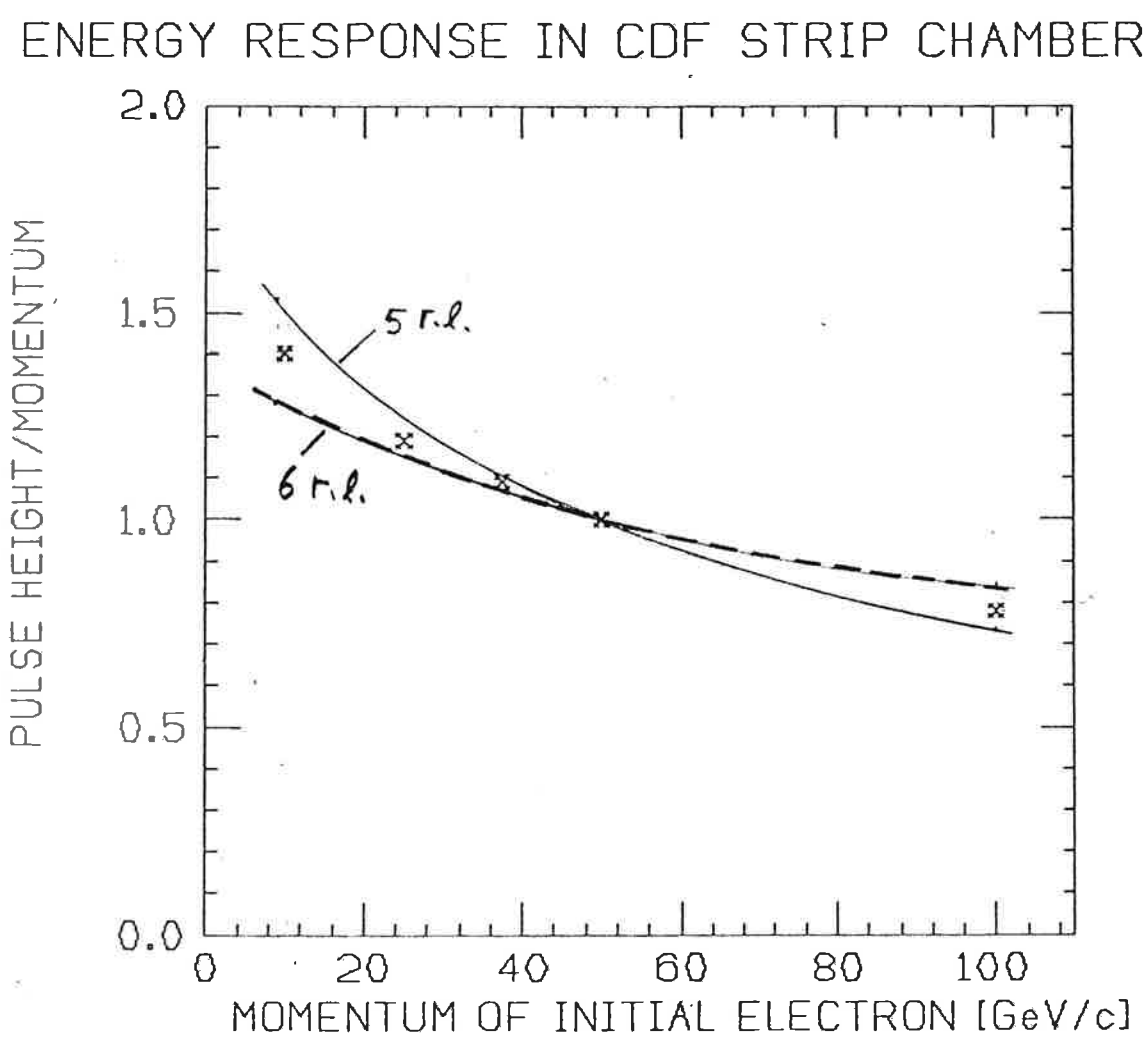
ENERGY RESPONSE IN CDF STRIP CHAMBER
PULSE HEIGHT/MOMENTUM
2.0
1.5
1.0
0.5
0.0
5 r.l.
6 r.l.
0
20
40
60
80
100
MOMENTUM OF INITIAL ELECTRON [GeV/c]

Fig. 1

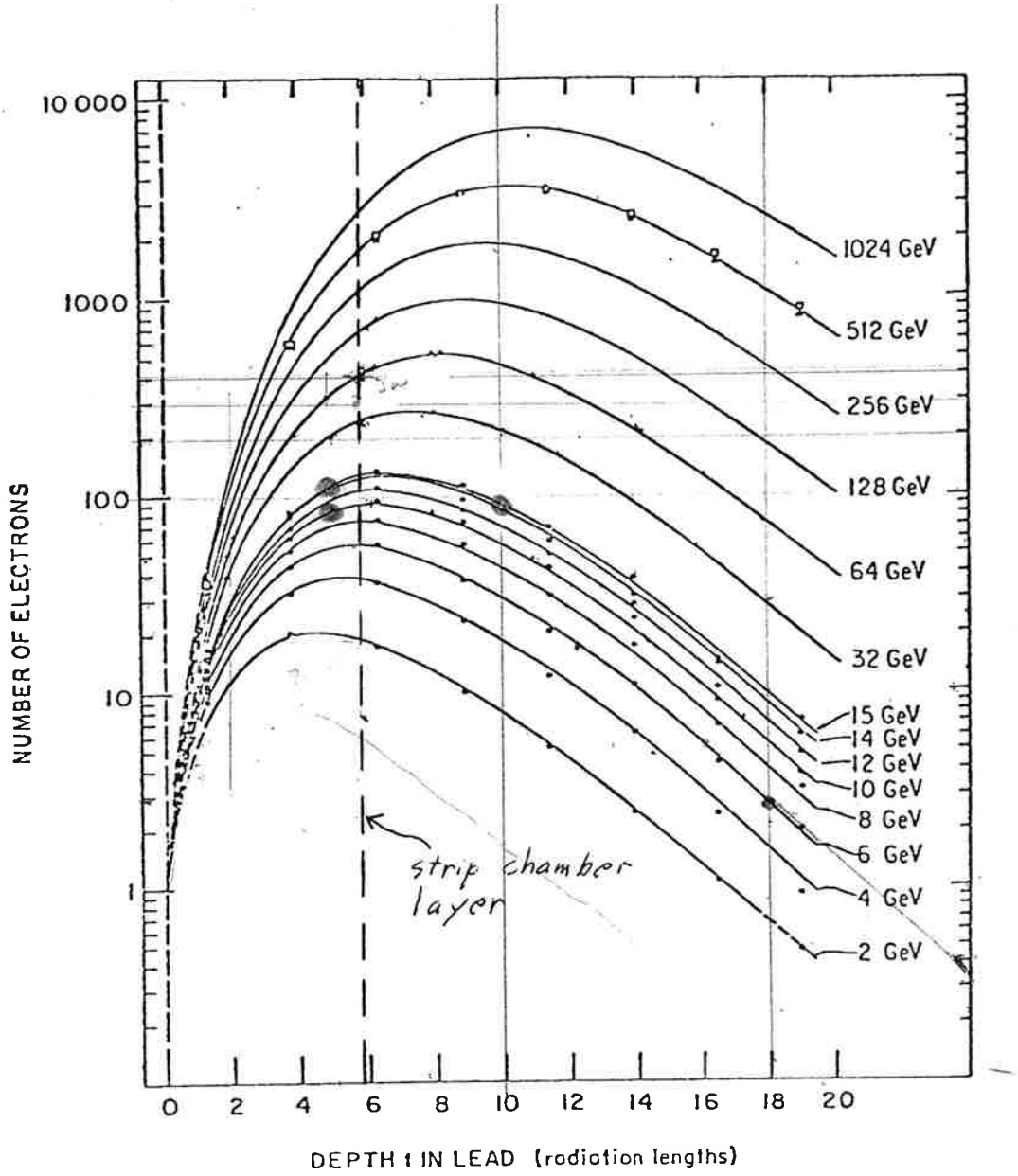
10 000
1000
100
10
1
NUMBER OF ELECTRONS
1024 GeV
512 GeV
256 GeV
128 GeV
64 GeV
32 GeV
15 GeV
14 GeV
12 GeV
10 GeV
8 GeV
6 GeV
4 GeV
2 GeV
strip chamber layer
0 2 4 6 8 10 12 14 16 18 20
DEPTH IN LEAD (radiation lengths)

Fig. 2

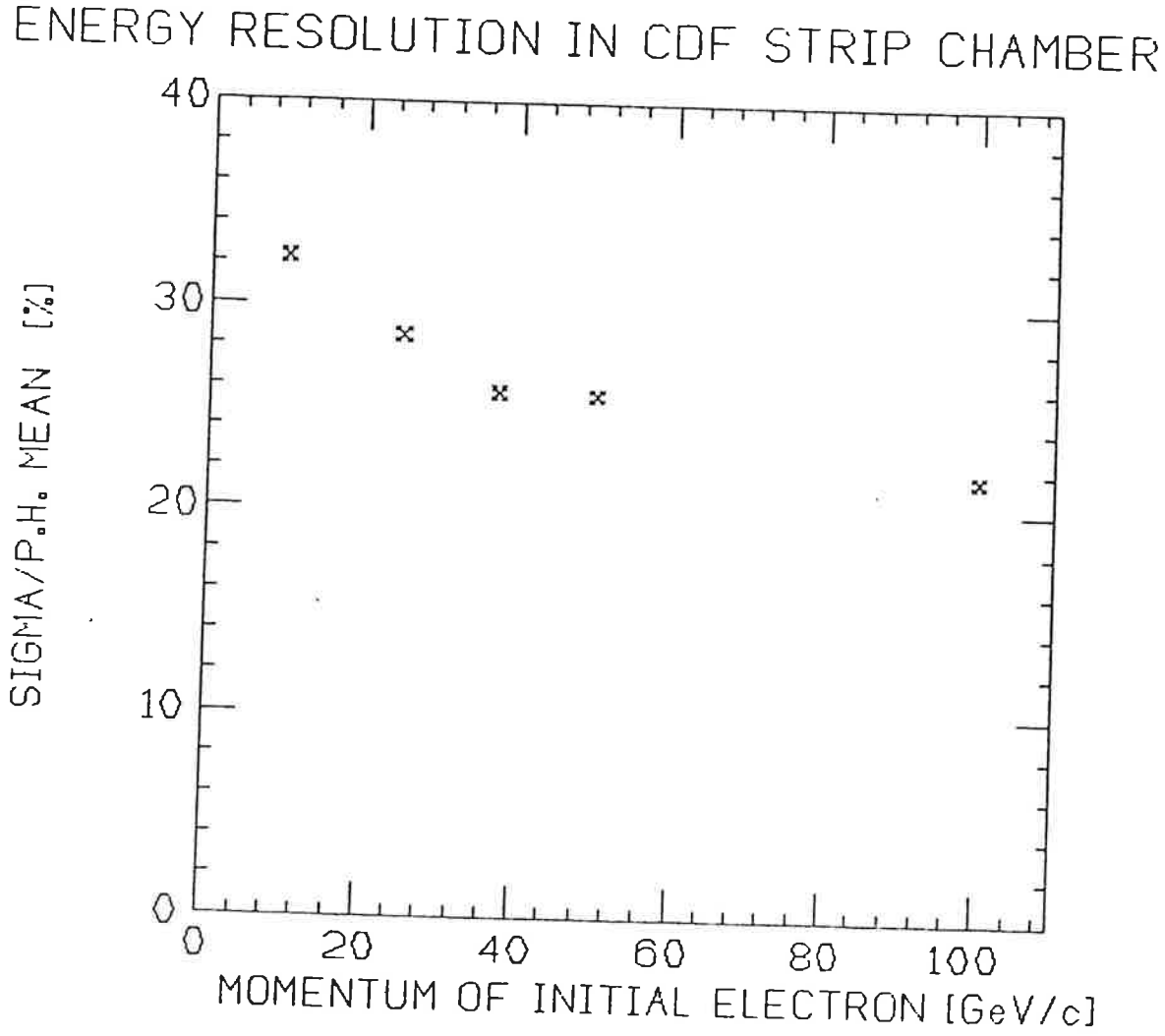
ENERGY RESOLUTION IN CDF STRIP CHAMBER
SIGMA/P.H. MEAN [%]
40
30
20
10
0
0
20
40
60
80
100
MOMENTUM OF INITIAL ELECTRON [GeV/c]

Fig. 3

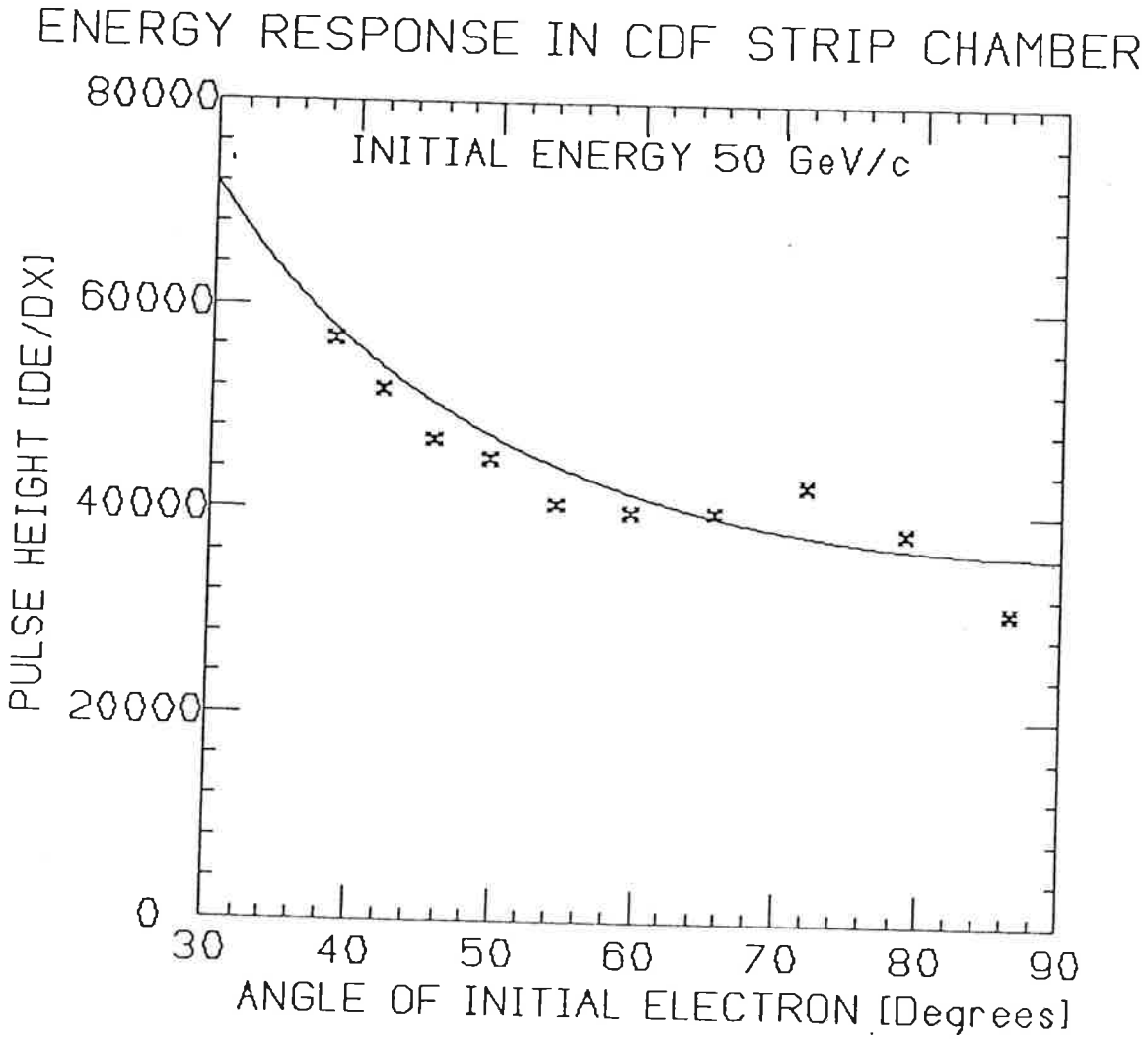
ENERGY RESPONSE IN CDF STRIP CHAMBER
INITIAL ENERGY 50 GeV/c
PULSE HEIGHT [DE/DX]
80000
60000
40000
20000
0
30
40
50
60
70
80
90
ANGLE OF INITIAL ELECTRON [Degrees]

Fig. 4

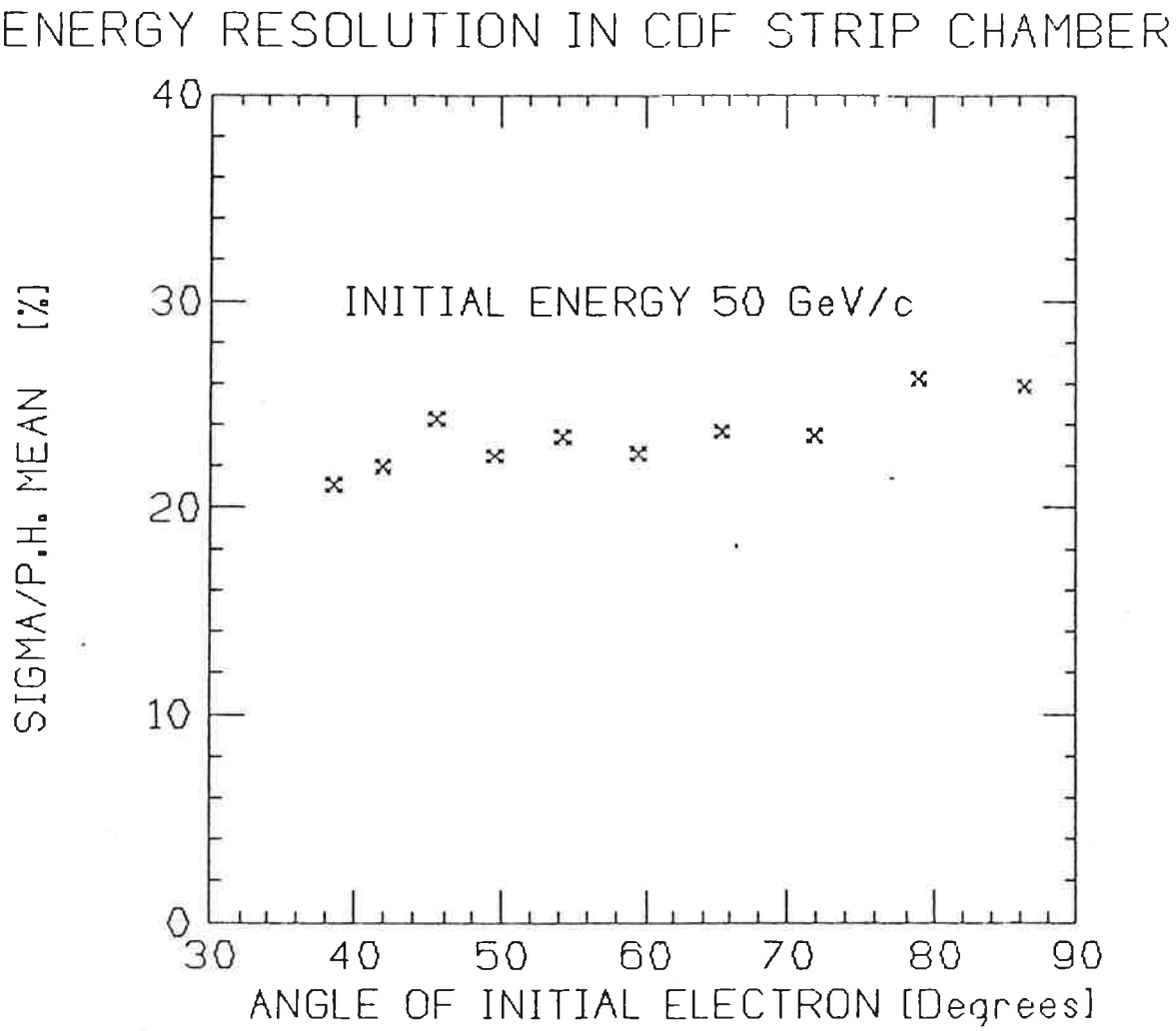
ENERGY RESOLUTION IN CDF STRIP CHAMBER
INITIAL ENERGY 50 GeV/c
SIGMA/P.H. MEAN [%]
ANGLE OF INITIAL ELECTRON [Degrees]
0
10
20
30
40
30
40
50
60
70
80
90

Fig. 5

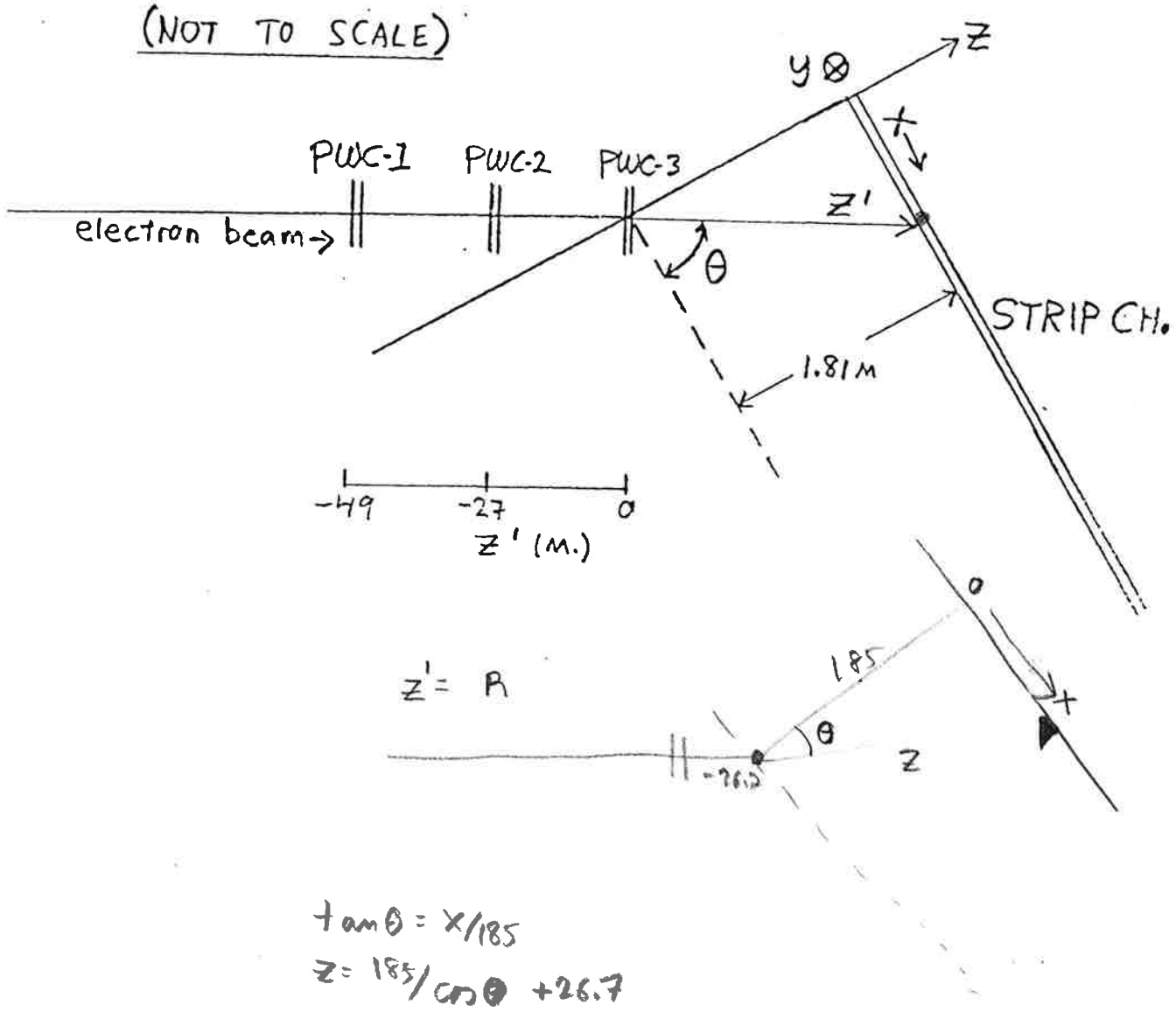
(NOT TO SCALE)
y ⊗
Z
x
PWC-1
PWC-2
PWC-3
Z'
electron beam→
θ
STRIP CH.
1.81 M
-49
-27
0
Z' (M.)
0
185
x
Z' = R
θ
Z
-26.7
tan θ = x/185
z = 185/cos θ +26.7

Fig. 6

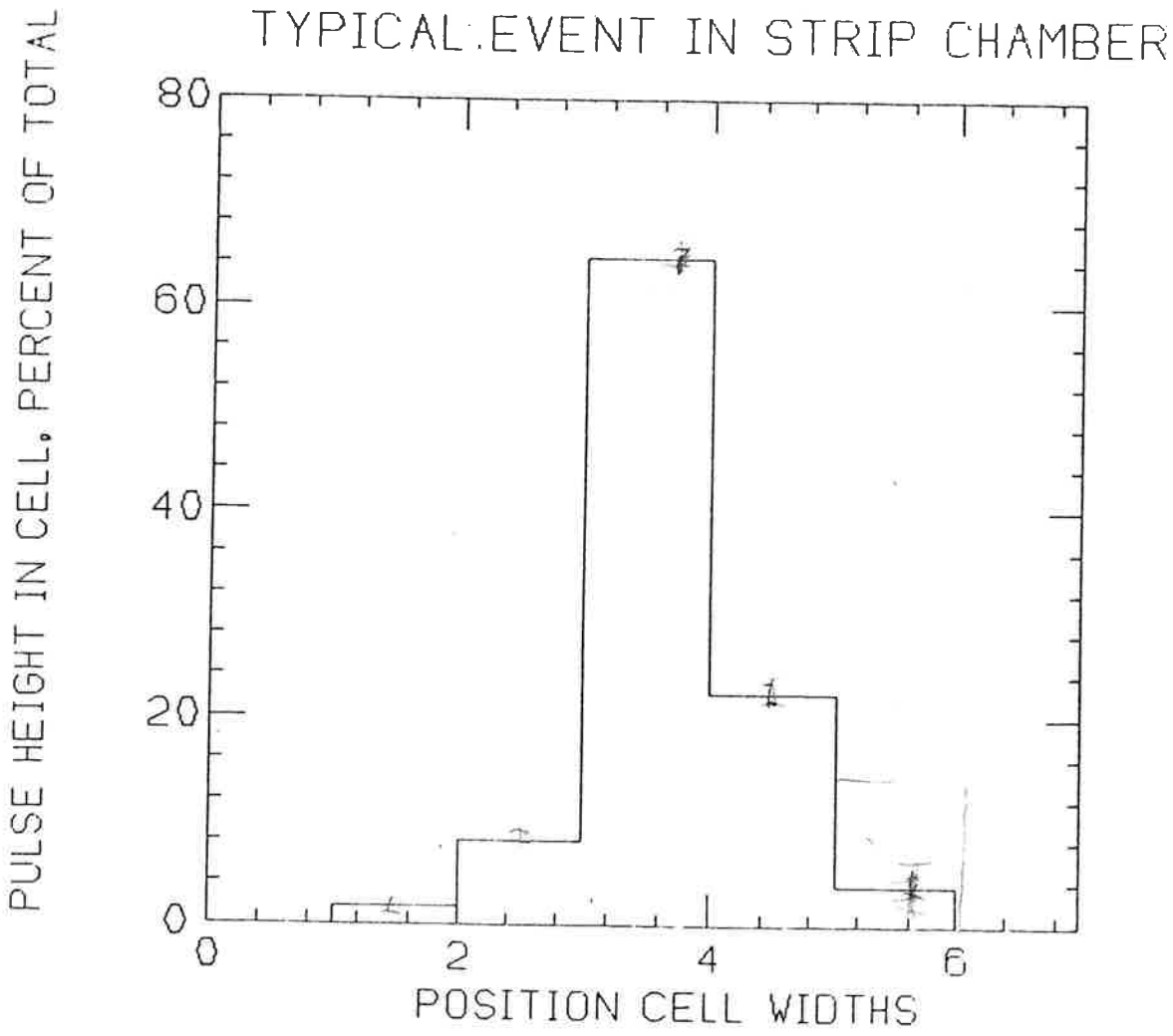
TYPICAL EVENT IN STRIP CHAMBER
PULSE HEIGHT IN CELL, PERCENT OF TOTAL
80
60
40
20
0
0
2
4
6
POSITION CELL WIDTHS

Fig. 7

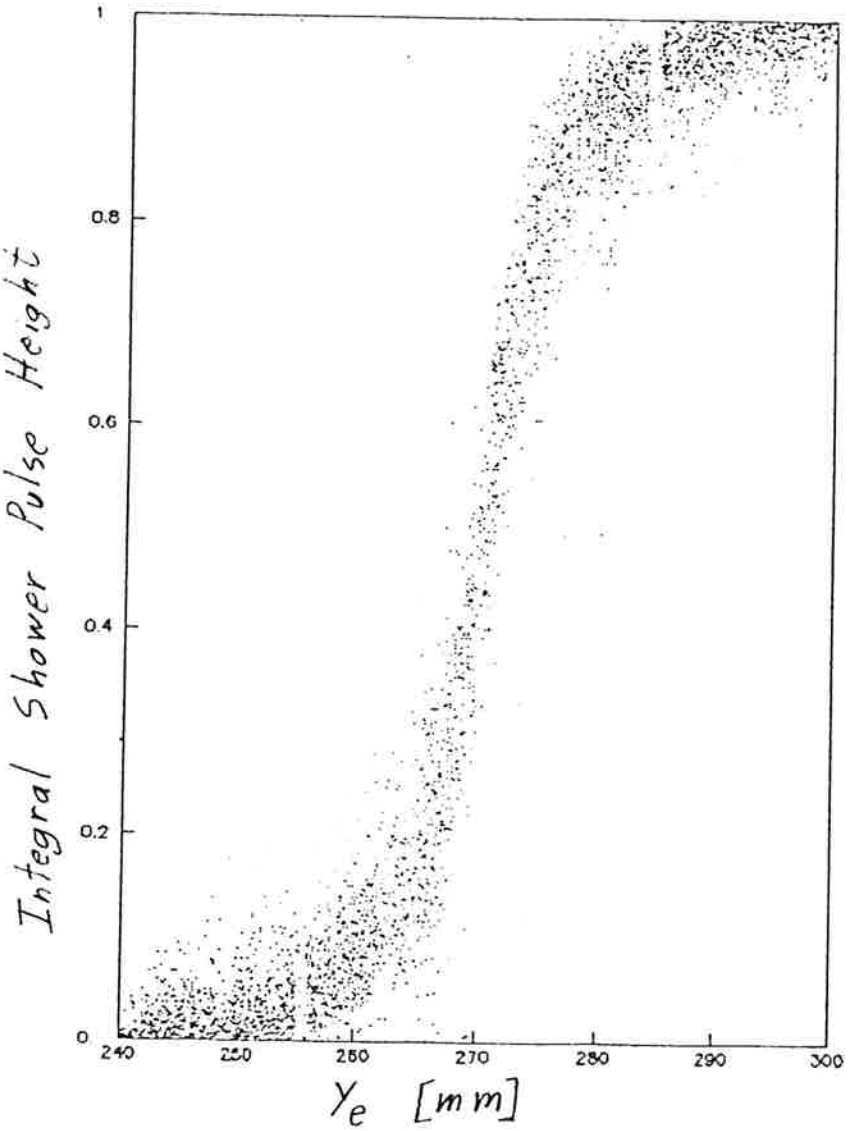
Integral Shower Pulse Height
1
0.8
0.6
0.4
0.2
0
240
250
260
270
280
290
300
Y_e [mm]

Fig. 8

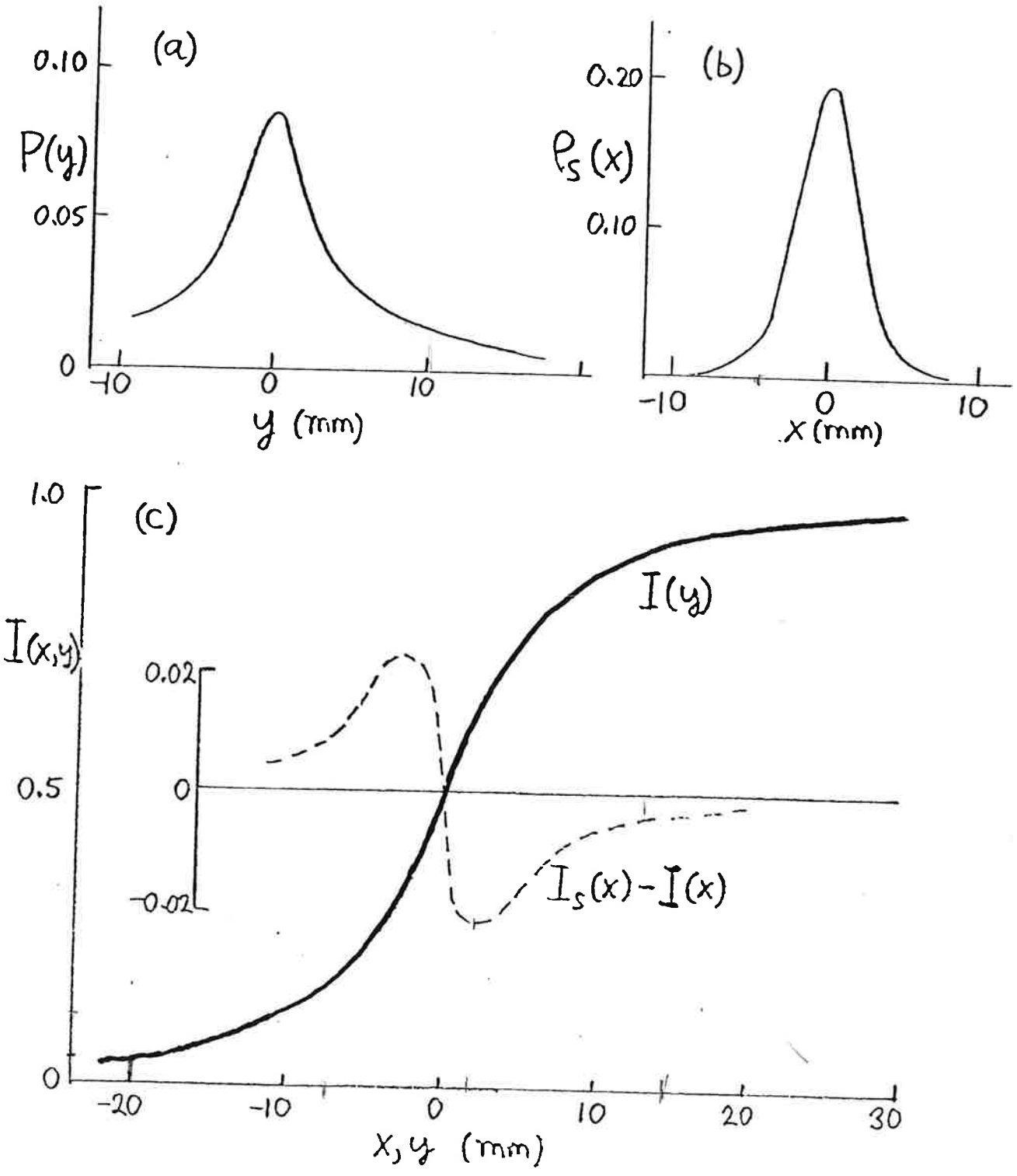
(a)
0.10
P(y)
0.05
0
-10
0
10
y (mm)
(b)
0.20
$\rho_s(x)$
0.10
-10
0
10
x (mm)
(c)
1.0
I(x,y)
0.5
0
0.02
0
-0.02
I(y)
$I_s(x) - I(x)$
-20
-10
0
10
20
30
x, y (mm)

Fig. 9

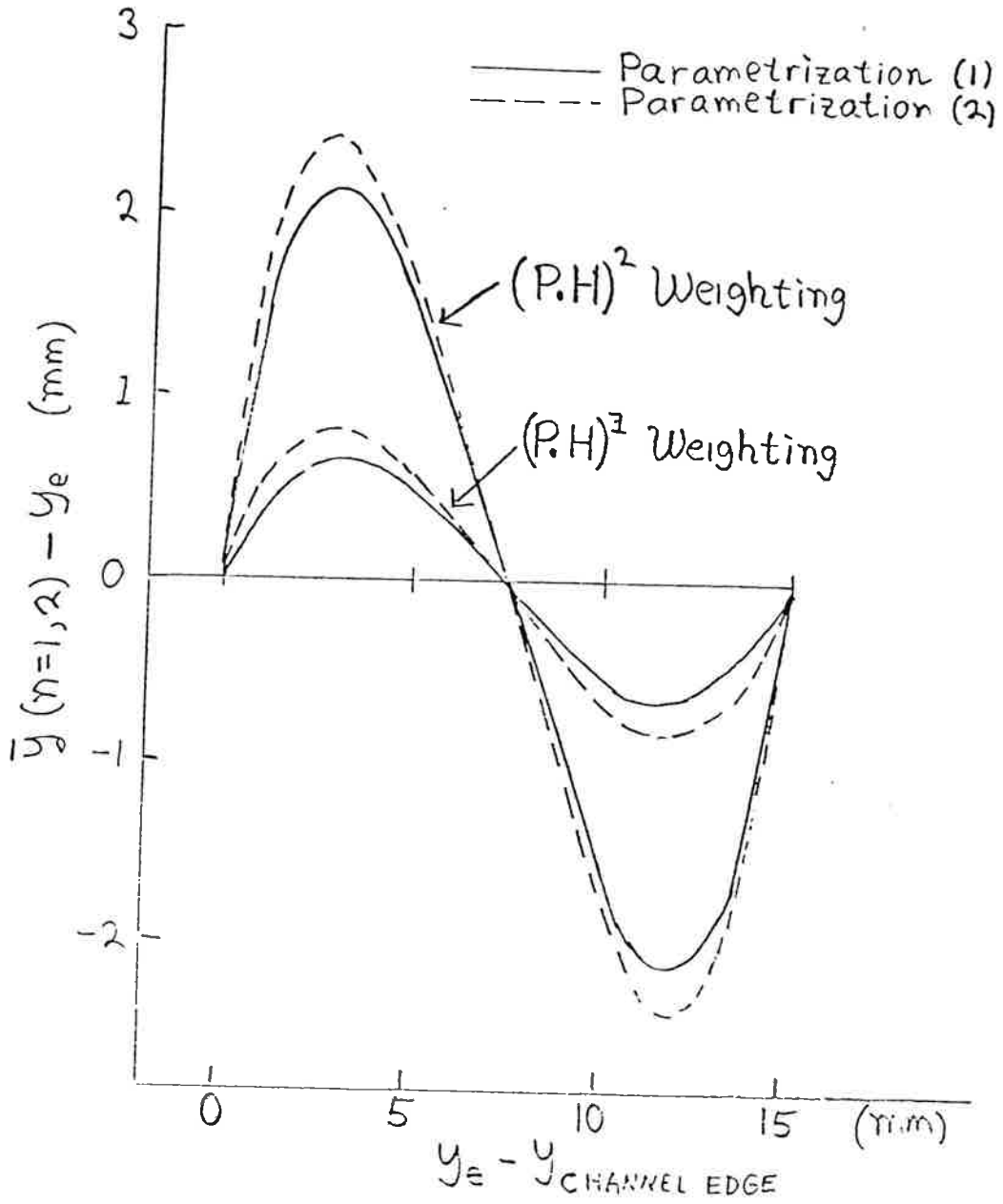
Parametrization (1)
Parametrization (2)
$(P.H)^2$ Weighting
$(P.H)^1$ Weighting
$\bar{y}_n (n=1,2) - y_e$ (mm)
3
2
1
0
-1
-2
0
5
10
15
(mm)
$y_e - y_{CHANNEL\ EDGE}$

Fig. 10

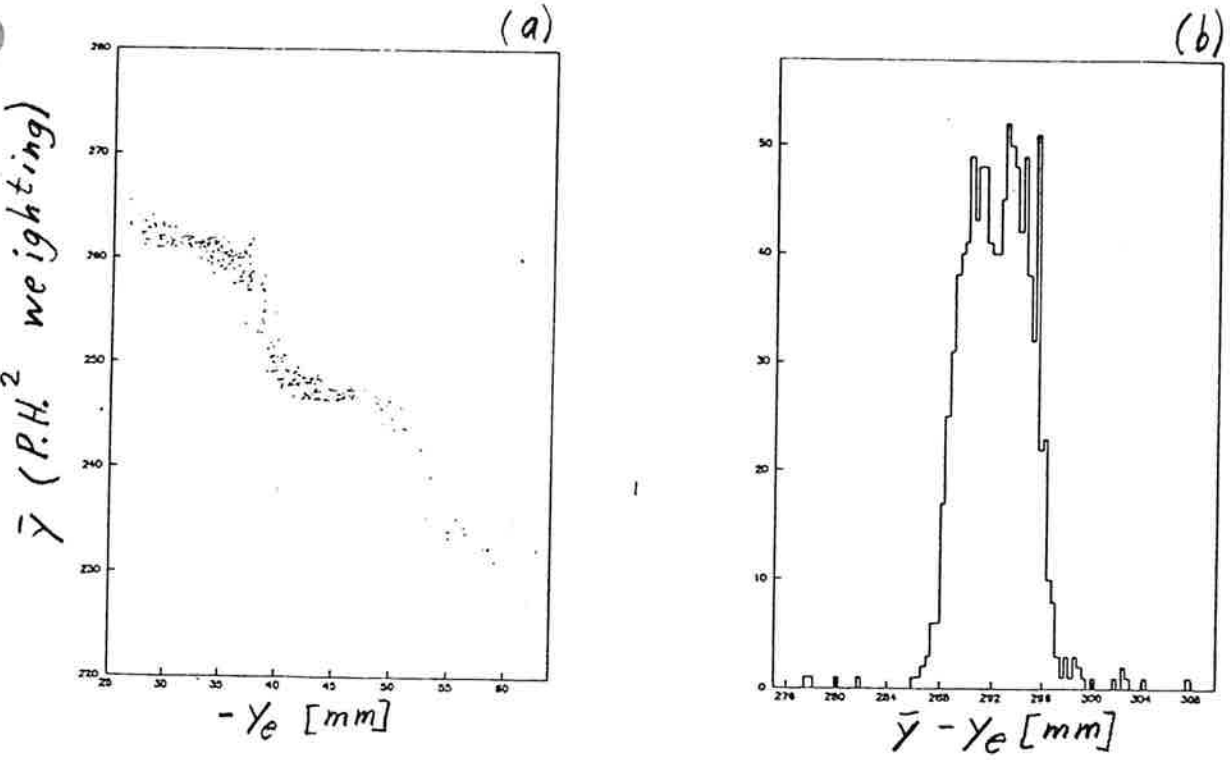
(a)
$\bar{y}$ (P.H.^{2} weighting)
$-Y_e$ [mm]
(b)
$\bar{y} - Y_e$ [mm]

Fig. 11

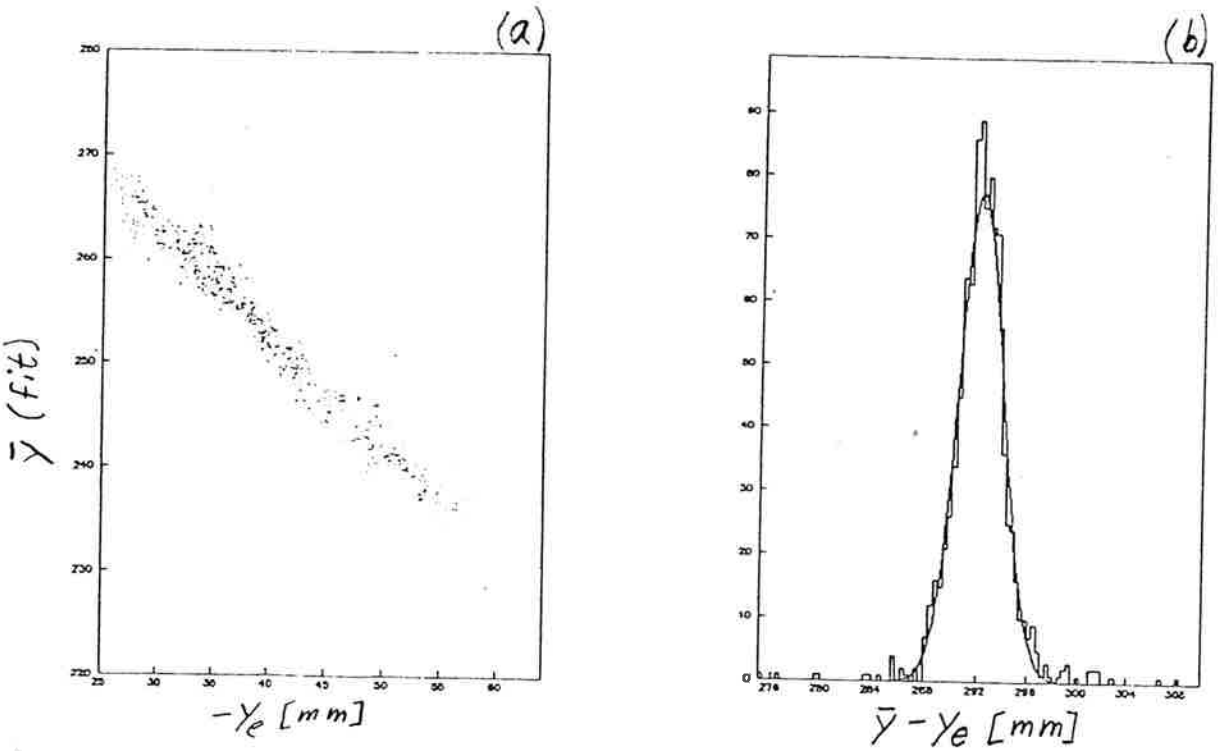
(a)
$\bar{y}$ (fit)
$-Y_e$ [mm]
(b)
$\bar{y} - Y_e$ [mm]

Fig. 12

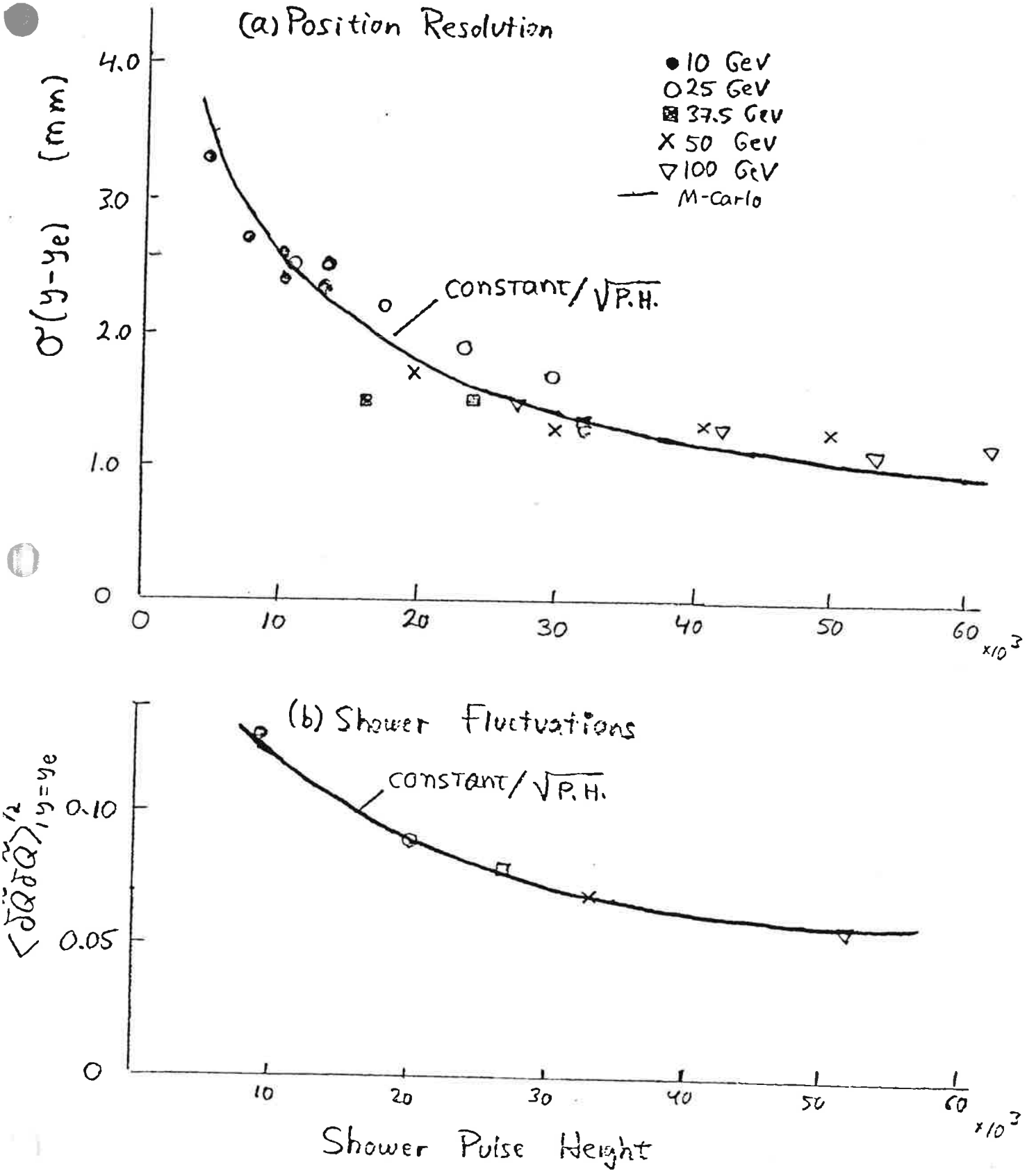
(a) Position Resolution
σ(y-ye) (mm)
4.0
3.0
2.0
1.0
0
10 GeV
25 GeV
37.5 GeV
50 GeV
100 GeV
M-Carlo
constant/√P.H.
0
10
20
30
40
50
60
x10³
(b) Shower Fluctuations
⟨δQ̃δQ̃⟩^½ y=ye
0.10
0.05
0
constant/√P.H.
10
20
30
40
50
60
x10³
Shower Pulse Height

Fig. 13

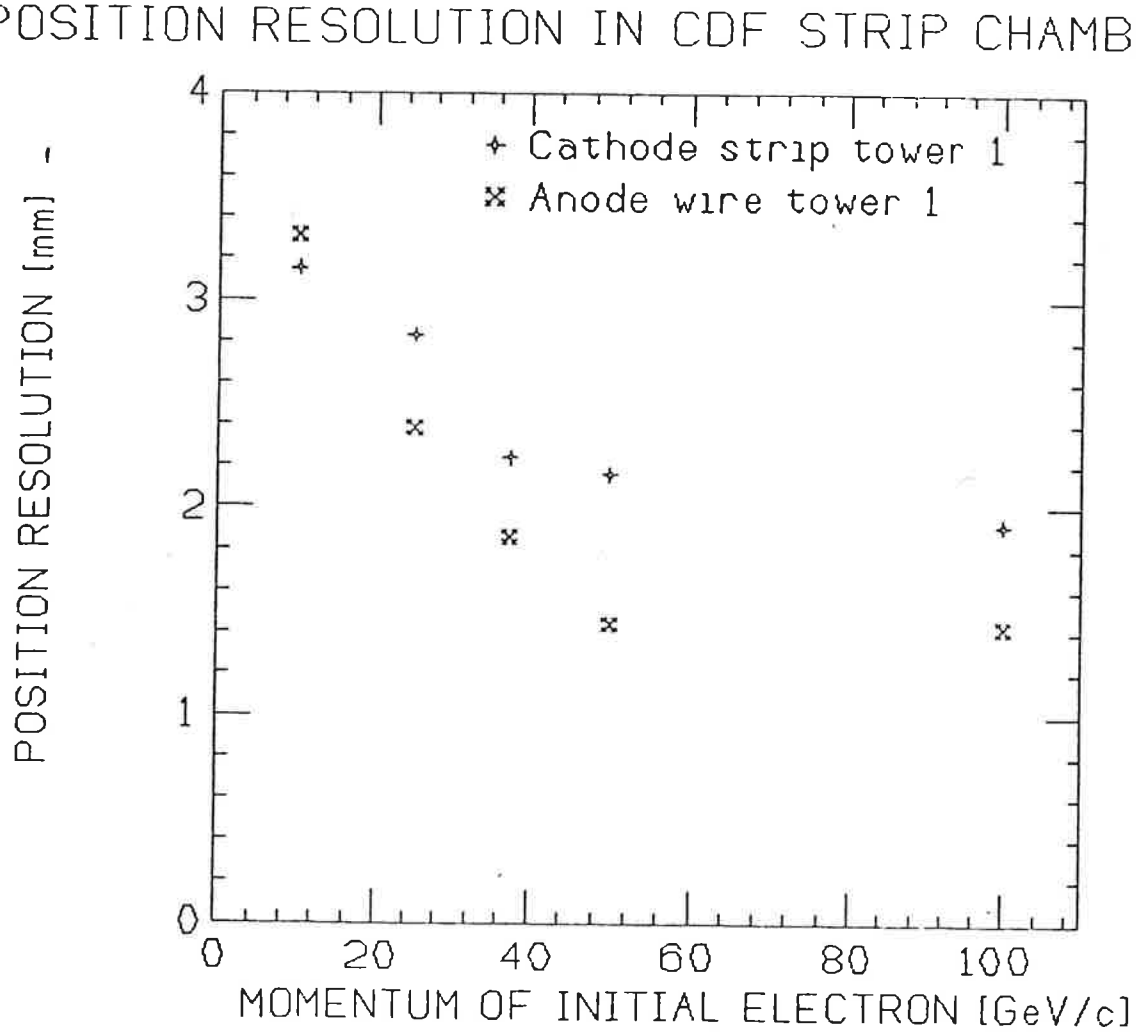
POSITION RESOLUTION IN CDF STRIP CHAMBER
Cathode strip tower 1
Anode wire tower 1
POSITION RESOLUTION [mm]
MOMENTUM OF INITIAL ELECTRON [GeV/c]
0
1
2
3
4
0
20
40
60
80
100

Fig. 14

POSITION RESOLUTION IN CDF STRIP CHAMBER

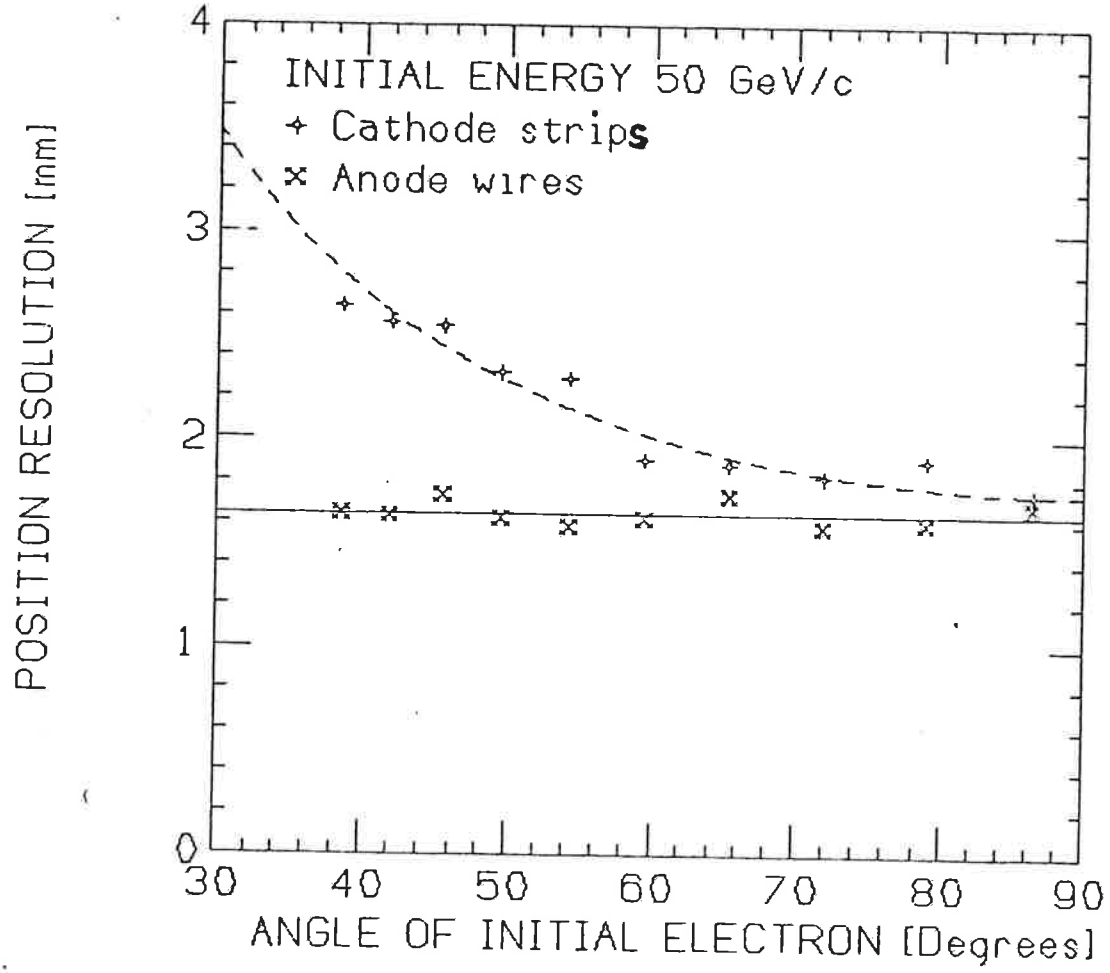

Fig. 15

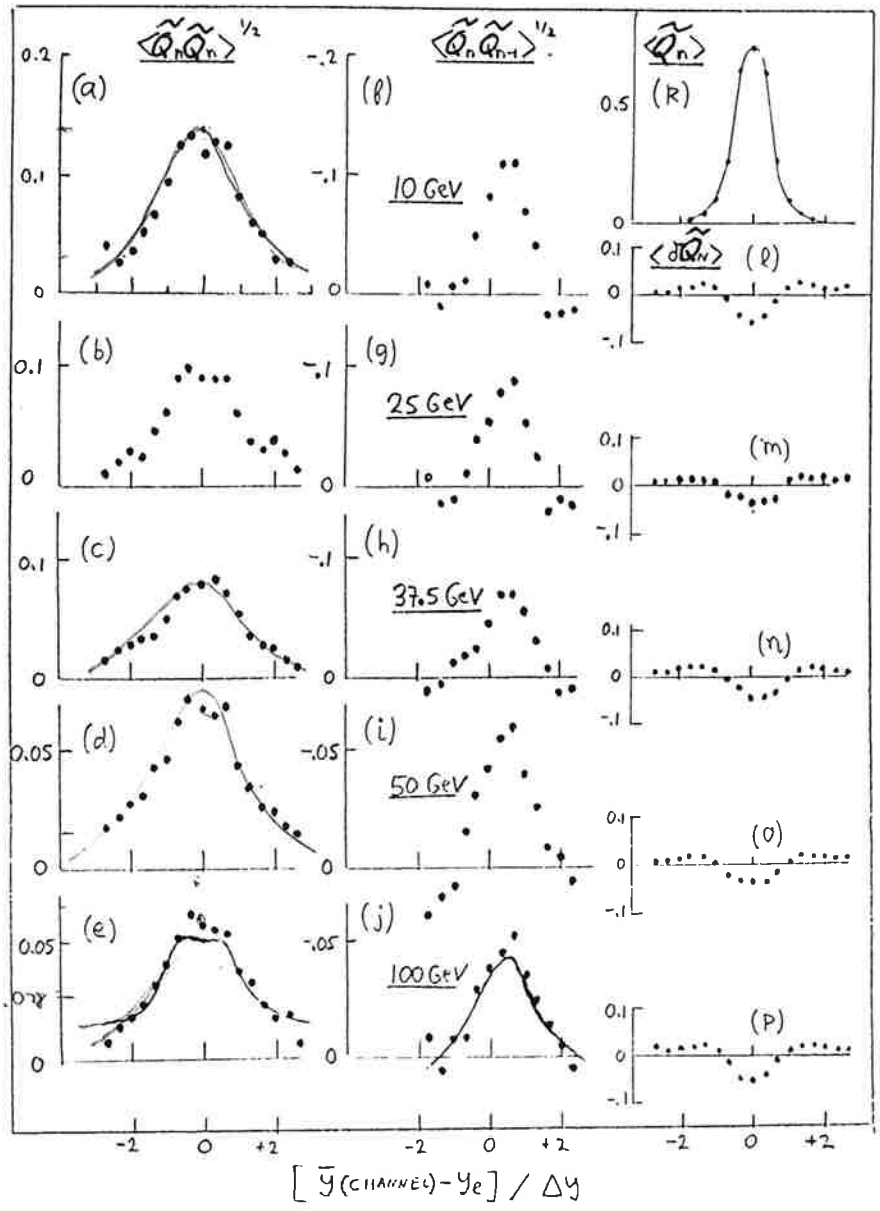
(a)
(b)
(c)
(d)
(e)
(f)
10 GeV
(g)
25 GeV
(h)
37.5 GeV
(i)
50 GeV
(j)
100 GeV
(k)
(l)
(m)
(n)
(o)
(p)
-2
0
+2
[ȳ(CHANNEL) - y_e] / Δy

.08

Fig. 16